Soil deformation measurement using particle image velocimetry (PIV) and photogrammetry

D. J. WHITE*, W. A. TAKE* and M. D. BOLTON*

A deformation measurement system based on particle image velocimetry (PIV) and close-range photogrammetry has been developed for use in geotechnical testing. In this paper, the theory underlying this system is described, and the performance is validated. Digital photography is used to capture images of planar soil deformation. Using PIV, the movement of a fine mesh of soil patches is measured to a high precision. Since PIV operates on the image texture, intrusive target markers need not be installed in the observed soil. The resulting displacement vectors are converted from image space to object space using a photogrammetric transformation. A series of validation experiments are reported. These demonstrate that the precision, accuracy and resolution of the system are an order of magnitude higher than previous image-based deformation methods, and are comparable to local instrumentation used in element testing. This performance is achieved concurrent with an order of magnitude increase in the number of measurement points that can be fitted in an image. The performance of the system is illustrated with two example applications.

KEYWORDS: centrifuge modelling; deformation; ground movements; laboratory equipment; laboratory tests; model tests

Nous avons développé un système de mesure des déformations basé sur la vélocimétrie d'image de particules (PIV) et la photogrammétrie rapprochée, pour l'utilisation dans les essais géotechniques. Dans cet article, nous décrivons la théorie à la base du système et nous validons sa performance. Nous utilisons la photographie numérique pour saisir les images de déformation planaires du sol. En utilisant la PIV, nous mesurons avec précision le mouvement de morceaux de sol à grains fins. Comme la PIV s'appuie sur la texture de l'image, il n'est pas nécessaire d'installer des marqueurs de cible intrusifs dans le sol observé. Nous convertissons les vecteurs de déplacement qui en résultent d'espace-image en espace-objet en utilisant une transformation photogrammétrique. Nous donnons les résultats d'une série d'essais de validation. Ceux-ci démontrent que la précision, l'exactitude et la résolution du système sont d'un ordre de grandeur plus élevé qu'avec les méthodes précédentes de déformation basées sur l'image et sont comparables à l'instrumentation locale utilisée dans les essais élémentaires. Nous obtenons cette performance en même temps qu'une augmentation de l'ordre de grandeur dans le nombre de points de mesure qui peuvent être placés dans une image. Nous illustrons la performance du système avec deux exemples d'applications.

INTRODUCTION

Deformation measurement in geotechnical testing

The assessment of soil behaviour in element tests or physical models at strain levels representative of prototype situations requires the detection of pre-failure strains. Modern techniques of local instrumentation have increased the precision of element test strain measurement into the small-strain (<0·001%) range (Scholey *et al.*, 1995). However, measurement techniques for the construction of planar deformation fields in geotechnical model tests remain less precise.

Various image-based techniques have been used to measure planar deformation fields in geotechnical element and model tests. These include X-ray (Roscoe *et al.*, 1963; Phillips, 1991) and stereo-photogrammetric methods (Butterfield *et al.*, 1970; Andrawes & Butterfield, 1973). More recently, the use of computer-based image processing techniques has led to the development of automatic target tracking systems (Taylor *et al.*, 1998; Paikowsky & Xi, 2000).

These experimental techniques rely on the presence of artificial targets—usually lead shot or coloured beads—within the deforming soil to provide reference points that are tracked as the element test or modelling event proceeds. The reliance on target markers has a number of drawbacks. A

dense grid of markers can influence the behaviour. A widely spaced grid of markers provides sparse data. Markers can become obscured by soil during the course of an experiment.

Performance: accuracy, precision and resolution

The performance of a measurement system can be assessed by considering the errors associated with accuracy, precision and resolution. Accuracy is defined as the systematic difference between a measured quantity and the true value. Precision is defined as the random difference between multiple measurements of the same quantity. Resolution is defined as the smallest interval that can be present in a reading.

The precision of a deformation measurement system based on the tracking of target markers depends on the method used to identify the location of the target within the photograph or digital image. The accuracy of the system depends on the process used to convert from the measured location within the image (image-space coordinates) to the location within the element or model test (object-space coordinates). Both precision and accuracy can be expressed in a non-dimensional fashion as a fraction of the width of the field of view (FOV).

By directly measuring the position of target markers on X-ray film, Phillips (1991) achieved a measurement precision of 1/10 000th of the FOV. Butterfield *et al.* (1970) and Andrawes & Butterfield (1973) achieved a comparable precision (1/11 000th of the FOV) using a stereo-photogrammetric method to measure photographic film. An advantage of the

stereo-photogrammetric method over conventional target-tracking techniques is that embedded markers are not required if soil grains can be distinguished. No assessment of accuracy was made in either case. Instead, it was assumed that image-space measurements could be scaled directly into object-space coordinates. In other words, it was assumed that the image scale—defined as the ratio between an object-space length and its length within the image or radiograph—was constant across the field of view.

Taylor *et al*. (1998) avoided the assumption of constant image scale by using close-range photogrammetry to reconstruct the object-space coordinates of target markers from the image-space measurements. An accuracy of 1/5600th of the FOV was achieved, when tracking target markers using video photography. Paikowsky & Xi (2000) used a second-degree polynomial fit to reconstruct object-space coordinates, and achieved an accuracy of 1/1266th of the FOV.

This paper describes the use of particle image velocimetry (PIV) and close-range photogrammetry to measure deformation in geotechnical models and element tests. The resulting performance is shown to exceed conventional image-based measurement techniques and offers precision and accuracy that are comparable to local instrumentation.

DIGITAL PHOTOGRAPHY

The measurement technique described in this paper operates by processing digital images, which can be captured directly from digital cameras or grabbed from an analogue video signal. In digitised form, a monochrome image is a matrix containing the intensity (brightness) recorded at each pixel on the camera's charge coupled device (CCD). This intensity matrix is defined as $I(\boldsymbol{U})$, where $\boldsymbol{U} = (u, v)$ is the pixel coordinate. Colour images consist of three intensity matrices, one for each colour channel.

Most geotechnical physical model and element tests take place sufficiently slowly to be captured by digital still cameras, which typically have a maximum frame rate of 0·1 Hz. These cameras offer better resolution and improved picture quality compared with video. The analogue transfer of video signals leads to image deterioration, and storage on tape creates line jitter. In contrast, digital still images undergo analogue–digital conversion within the camera, preventing the addition of noise during transfer and storage stages. The images analysed in this paper were captured using a Kodak DC280 digital still camera, which has an image resolution of 1760 × 1168 pixels.

PARTICLE IMAGE VELOCIMETRY (PIV)
Theory

PIV is a velocity-measuring technique that was originally developed in the field of experimental fluid mechanics (Adrian, 1991). The technique was originally implemented using double-flash photography of a seeded flow. The resulting photographs contain image pairs of each seed particle. For PIV analysis, the photograph is divided into a grid of test patches. The displacement vector of each patch during the interval between the flashes is found by locating the peak of the autocorrelation function of each patch. The peak in the autocorrelation function indicates that the two images of each seeding particle captured during the flashes are overlying each other. The correlation offset is equal to the displacement vector.

A modified approach has been used to implement PIV in geotechnical testing. Whereas fluid requires seeding with particles to create features upon which image processing can operate, natural sand has its own texture in the form of different-coloured grains and the light and shadow formed between adjacent grains when illuminated. Texture can be added to an exposed plane of clay by the addition of coloured 'flock' material or dyed sand.

The image processing conducted during PIV to measure the displacement between a pair of digital images is shown schematically in Figs 1 and 2. The first image is divided into a grid of test patches. Each test patch, $I_{\text{test}}(\boldsymbol{U})$, consists of a sample of the image matrix, $I(\boldsymbol{U})$, of size $L \times L$ pixels.

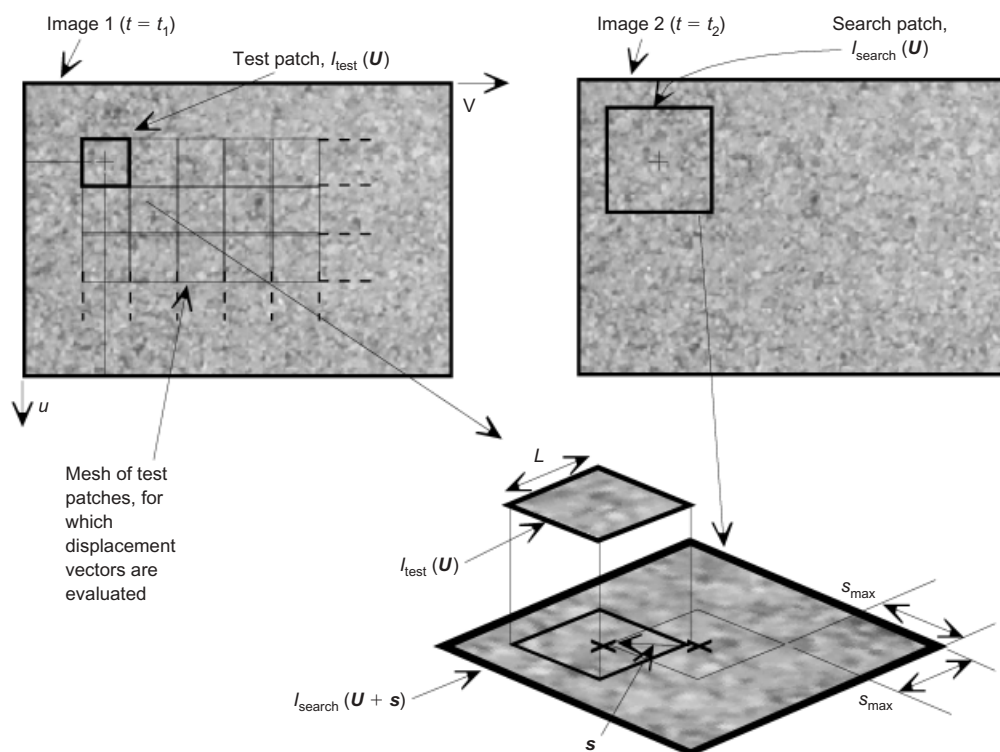To find the displacement of the test patch between images

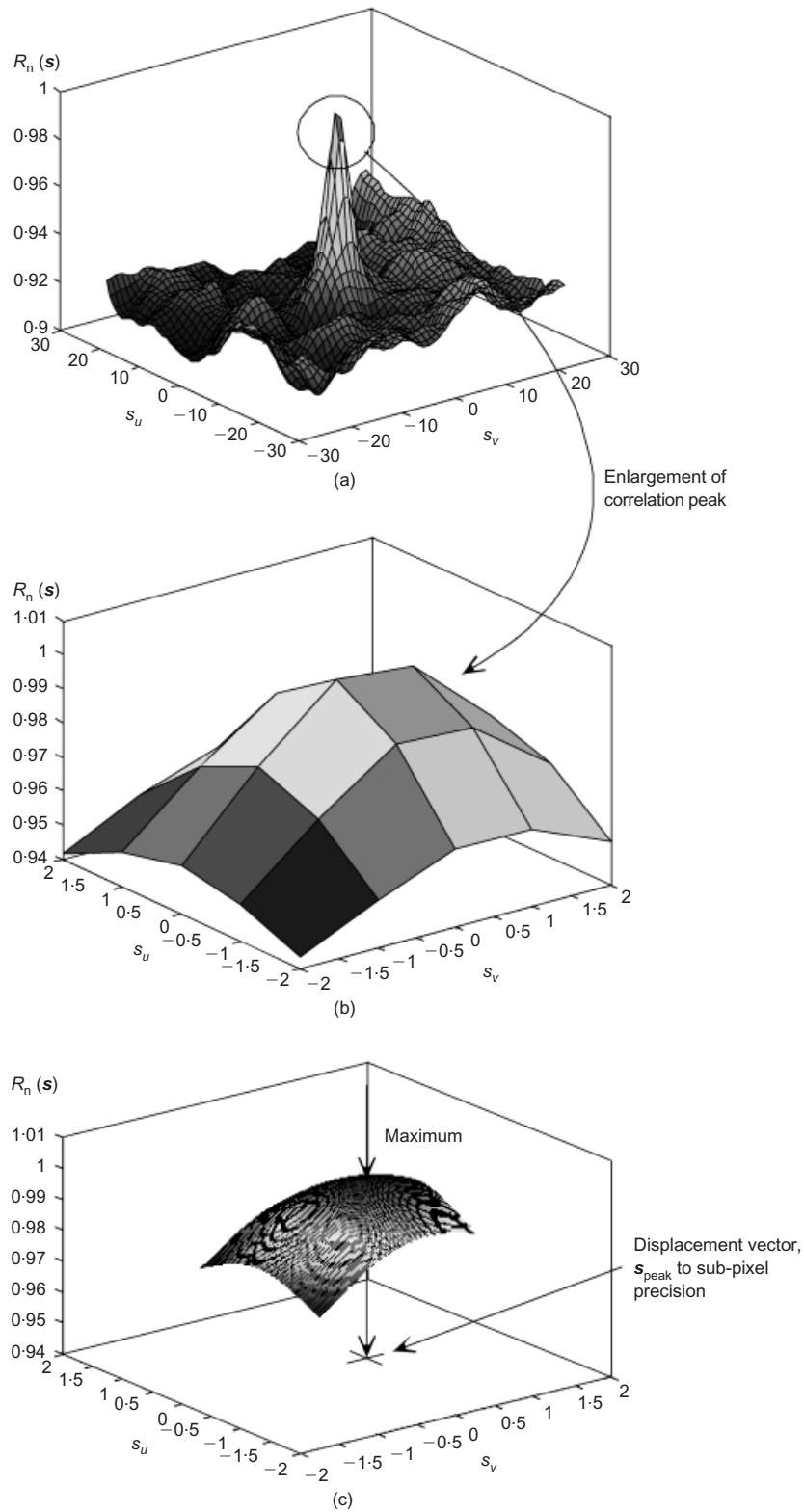Fig. 1. Image manipulation during PIV analysis

Fig. 2. Evaluation of displacement vector from correlation plane, $R_n(s)$: (a) correlation function $R_n(s)$; (b) highest correlation peak (integer pixel); (c) sub-pixel interpolation using cubic fit over ±1 pixel of integer correlation

1 and 2, a search patch $I_{search}(\mathbf{U} + \mathbf{s})$ is extracted from the second image. This search patch extends beyond the test patch by a distance s_{max}, in the u and v directions, defining the zone in which the test patch is to be searched for (Fig. 1). The cross-correlation of $I_{test}(\mathbf{U})$ and $I_{search}(\mathbf{U} + \mathbf{s})$ is evaluated, and normalised by the square root of the sum of the squared values of $I_{search}(\mathbf{U} + \mathbf{s})$ over the range of $\mathbf{U}$ occupied by the test patch. The resulting normalised correlation plane $R_n(s)$ indicates the 'degree of match' between the test and search patch over the offset range in the domain of $\mathbf{s}$ (Fig. 2(a)). To reduce the computational requirement, the correlation operations are conducted in the frequency domain by taking the fast Fourier transform (FFT) of each patch and following the convolution theorem.

The highest peak in the normalised correlation plane, $R_n(s)$, indicates the displacement vector of the test patch, s_{peak} (Fig. 2(b)). The correlation plane is evaluated at single pixel intervals. By fitting a bicubic interpolation to the region close to the integer peak, the displacement vector is established to sub-pixel resolution (Fig. 2(c)). Generally, the bicubic interpolation function is evaluated at 1/200th pixel intervals, yielding a system resolution of 0·005 pixels. To improve the resolution, a smaller interval can be selected, with a corresponding increase in computational burden. However, a resolution greater than 0·005 pixels is unnecessary since in most cases the errors associated with accuracy and precision are larger.

The flowchart for PIV analysis of an image series is shown in Fig. 3. The procedure described above for evaluating a single displacement vector is repeated for the entire grid of test patches, producing the displacement field between the image pair. The analysis is continued by substituting the second image ($t = t_2$) with a subsequent image ($t = t_3$). The analysis is repeated by comparing the first and third images. As the analysis continues, distortion of the viewed soil or changes in lighting may reduce the sharpness of the correlation peak that identifies the displaced location of a given PIV patch. If the correct correlation peak is drowned by random noise on the correlation plane an incorrect, or 'wild', vector will be recorded. To eliminate this possibility, the 'initial' image, in which the test patches are established, is updated at intervals during the analysis.

Assessment of PIV performance

A series of experiments was conducted to assess the precision of PIV. These experiments involved the controlled rigid-body movement of a planar body below a fixed camera. In each case, a mesh of test patches was established on the planar body, and an image pair were compared. The random variation in the recorded displacement vectors indicates the precision of the measurement technique; ideally all the vectors would be identical during a rigid body translation.

The series of experiments investigated the following influences on PIV precision:

(*a*) test patch size
(*b*) soil type/appearance
(*c*) movement distance: whole or fraction of a pixel.

The first experiment, A, used an artificial image of soil, consisting of a matrix of randomly generated pixel intensities, in the range 0 to 255. This random image allows the 'soil' movement to be exactly controlled, and makes it possible to remove any image changes due to lighting or camera shake. Fig. 4(a) shows a sample of this random image, with an enlargement of a 10×10 pixel test patch.

A series of seven PIV analyses were conducted, in which the entire 500×500 pixel random image was covered in square test patches with side length, L, of 6, 8, 10, 16, 24, 32 and 50 pixels respectively. The analysis was conducted by comparing the random image with itself—that is, over a rigid body displacement increment of zero pixels. The scatter of displacement measurements recorded during comparison of a random image with itself is identical to that which would be recorded had a new 'displaced' image been created by cropping one side of the original image. The correlation plane would be identical, but displaced by an amount equal to the artificial image shift.

Therefore the results of this initial experiment, although conducted over an image displacement of zero pixels, correspond to any integer pixel rigid-body translation of an artificial soil image, in which the brightness of each pixel is random, and independent of its neighbours.

Each PIV analysis revealed a scatter of values, distributed close to zero. Larger PIV patches produced less scatter, and therefore improved precision. By plotting the standard deviation in measured displacement against test patch size, the influence of patch size on measurement precision can be seen (Fig. 5). Curve A shows the results from the seven PIV
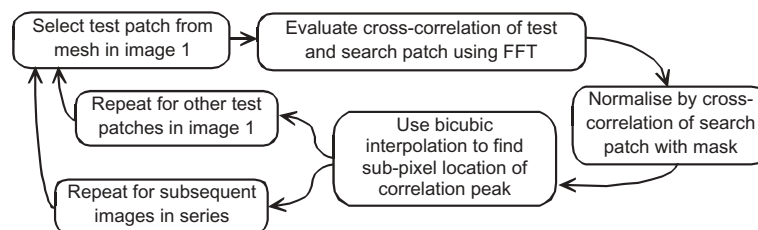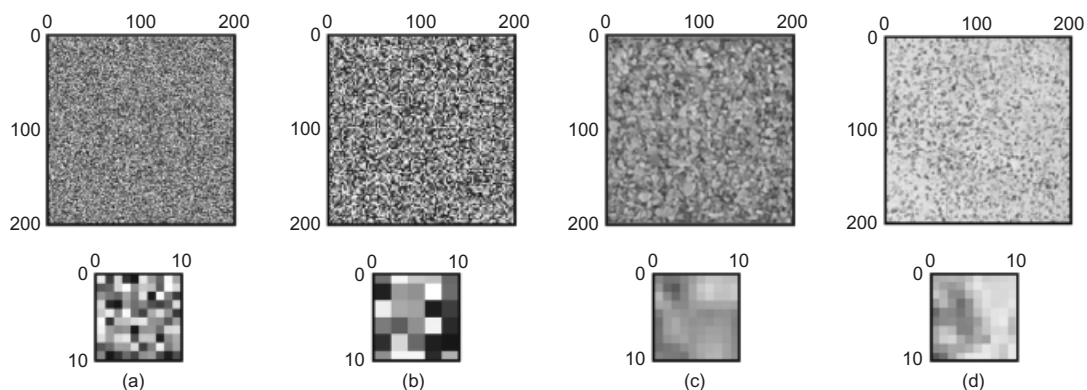

Fig. 3. Flowchart of PIV analysis

Fig. 4. Images used in PIV validation experiments (axes in pixels): (a) random image; (b) random image, 2×2 'grains'; (c) Dog's Bay sand; (d) kaolin clay with artificial texture
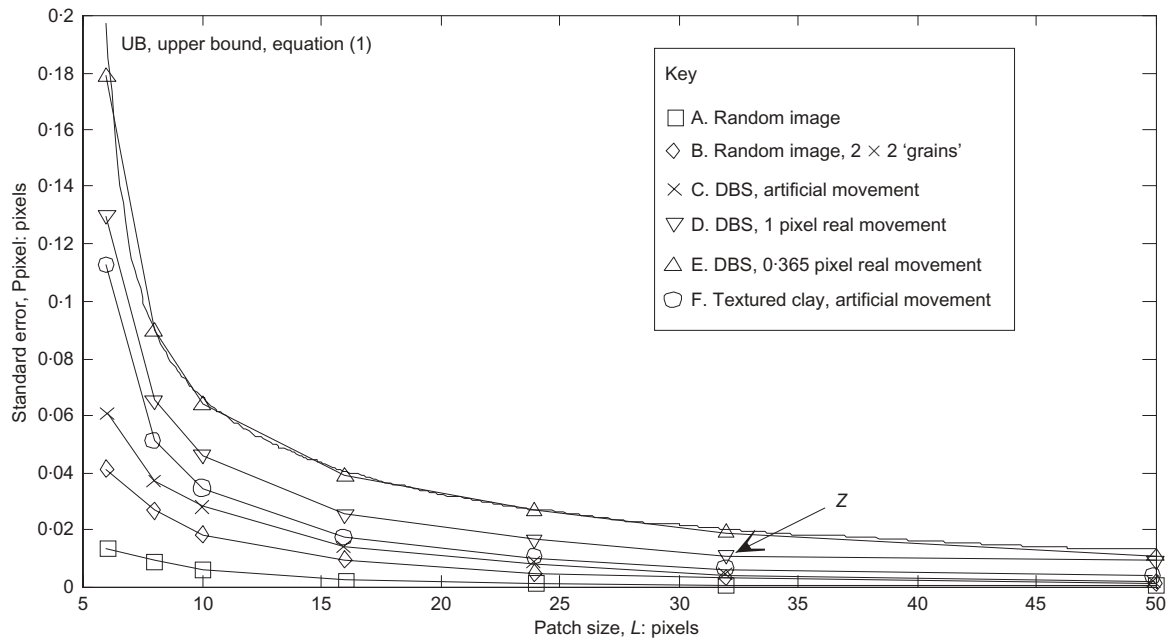
Fig. 5. PIV precision against patch size

analyses of the random image, revealing a precision better than 0·01 pixels for patches greater than 8×8 pixels in size. The largest PIV patches, of size 50×50 pixels, were distributed around zero with a standard error of 0·0007 pixels. In order for these analyses to be a test of the measurement precision rather than the measurement resolution, the sub-pixel correlation peak was evaluated at intervals of 1/10 000th of a pixel, rather than 1/200th.

These precision errors are associated with asymmetry of the correlation peak. In the case of this random image, the height of the correlation peak prior to interpolation, expressed mathematically as the value of $R_n(s)$ for $s = 0$, is unity, as an identical match for the test patch exists in the search patch. In the case of this entirely random image, the values of $R_n(s)$ one pixel to either side of the peak lie in the 'sea' of random noise in which no positive correlation exists between the test patch and the underlying region of the search patch. If the values of $R_n(s)$ on either side of the peak were identical, the interpolated correlation peak would be symmetrical and the sub-pixel peak would lie at the integer value. In contrast, if these values differ, the interpolated peak is asymmetric, and the small random errors shown in curve A, and associated with measurement precision, are created.

The discussion above demonstrates that a very high measurement precision can be obtained using a random 'soil' image, as a very sharp correlation peak is created. However, real images of soil are not entirely random. The brightnesses of neighbouring pixels are not independent, as they may depict parts of the same grain. Expressed mathematically, the spatial brightness frequency of a soil image is lower. Neighbouring pixels are of similar colour.

A second experiment was conducted to examine the influence of spatial brightness frequency. The random image used in experiment A was artificially enlarged such that blocks of $4 (2 \times 2)$ pixels were of identical brightness. The resulting image, of size 1000×1000 pixels, was analysed in the same fashion as described previously, using test patch sizes varying from 6×6 to 50×50 pixels. A section of the image, and a typical 10×10 test patch, are shown in Fig. 4(b).

The results, shown as curve B in Fig. 5, revealed a reduced precision, compared with the entirely random image. The precision errors associated with each patch size are increased by a factor of 3, with 10×10 pixel patches exhibiting a scatter of 0·0183 pixels. This reduced precision is once again associated with the shape of the sub-pixel correlation peak. Although a perfect match exists at $s = 0$, the adjacent values of $R_n(s)$ are no longer in the random sea of the correlation plane; some positive correlation exists at an offset of one pixel as the 'grains' are now of size 2×2 pixels. The resulting interpolated correlation peaks are less sharp, are asymmetric, and lead to reduced precision.

Experiment C used a real image of Dog's Bay sand. This image was taken at a nominal image scale of 0·1 mm/pixel, giving a FOV of 176 mm $\times$ 112 mm (Fig. 4(c)). This FOV was chosen as it is comparable to the model testing for which this system was developed. The D_{50} size of the sand was found to be 0·44 mm by sieving.

In order to continue to isolate the influence of image type from possible precision errors due to non-rigid body motion, lighting changes or camera shake, experiment C compared the image of Dog's Bay sand with itself, for various patch sizes (curve C in Fig. 5). A further reduction in precision compared with the random 2×2 'grain' image is evident.

Experiment D introduced the influence of random changes in appearance associated with taking multiple photos of a translating object. These changes in appearance arise due to lighting changes and random variations in CCD sensitivity. The tray of sand was translated below the fixed camera using a micrometer. A series of images was captured, at displacement increments corresponding to both integer and fractions of a pixel. Experiment D compared two images of Dog's Bay sand between which the tray of sand was translated by (nominally) one pixel. Fig. 6(a) shows the entire image, including the translating tray and micrometer, with the mesh of 32×32 pixel test patches superimposed. The measured displacement field is shown in Fig. 6(b).

Curve D shows the standard error in recorded displacement for each patch size. The mean value of recorded displacement was 1·0017 pixels; there was a discrepancy of
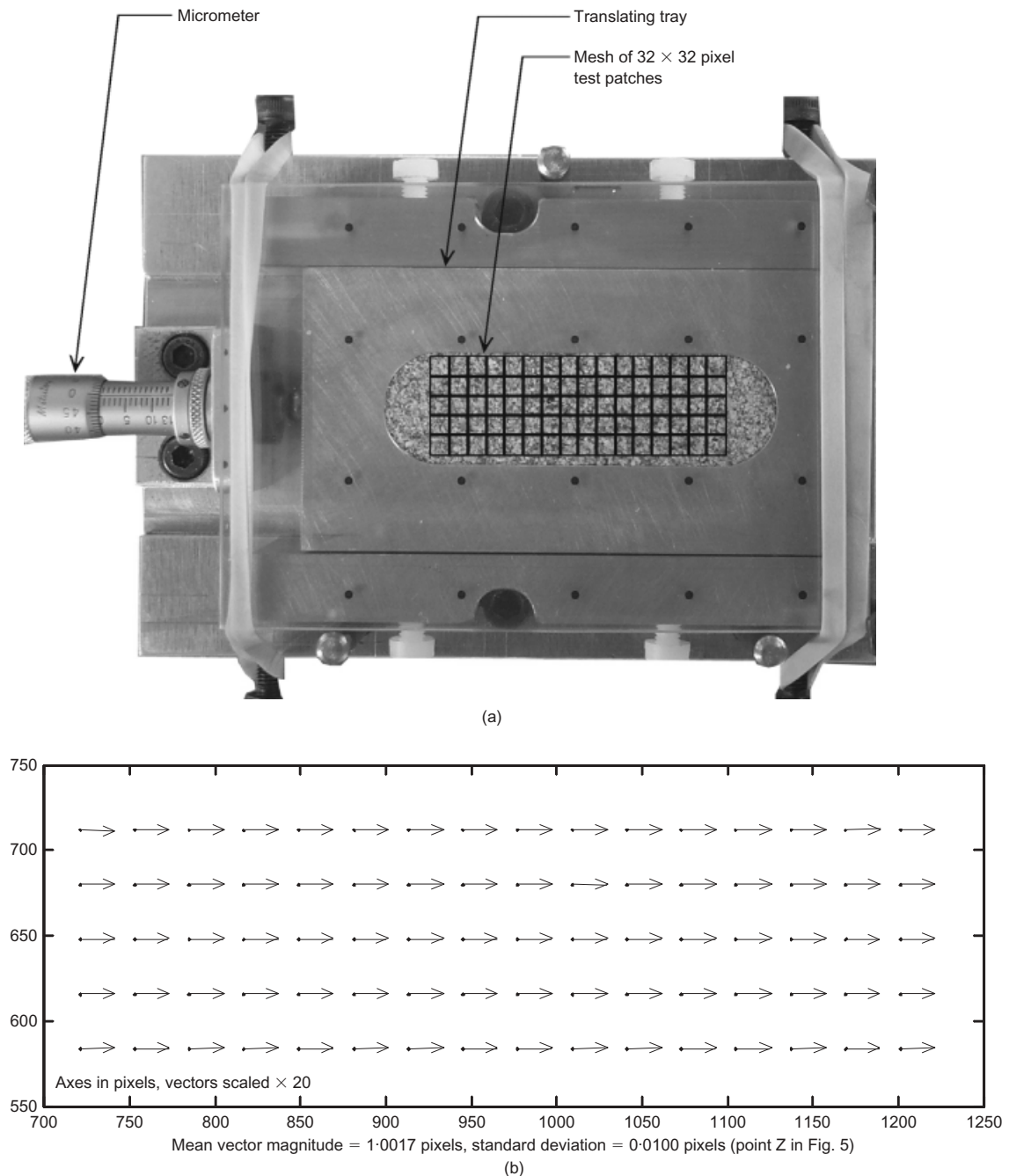
(a)

Mean vector magnitude = 1·0017 pixels, standard deviation = 0·0100 pixels (point Z in Fig. 5)

(b)

Fig. 6. Precision validation experiment D: (a) translating tray containing Dog's Bay sand; (b) measured displacement vectors

~0·3 μm between the desired one pixel movement and the actual movement that was manually applied via the micrometer.

In experiment D, a reduction in precision compared with experiment C was recorded. The random errors associated with multiple images increased the standard error for 10×10 pixel PIV patches to 0·0460 pixels.

Experiments A–D considered displacement increments equal (or very close) to an integer value. Experiment E compared two images between which the tray of sand was translated by 0·365 pixels, to examine the precision associated with displacements of a fraction of a pixel. Curve E shows the recorded errors, which indicate a further reduction in precision; the standard error for 10×10 pixel PIV patches is 0·0642 pixels. These results indicate that precision is reduced when interpolating far from an integer value;

greater reliance is placed on the sub-pixel bicubic interpolation.

Experiment F examined the possibility of imparting artificial texture to clay, which is otherwise not suitable for image analysis, being of uniform brightness. Fig. 4(d) shows an image of kaolin clay dusted with fine dyed sand. This image was compared with itself, in the manner of experiment C for Dog's Bay sand. The resulting precision (curve F) is comparable to experiment C, indicating that the analysis technique is as applicable to artificially textured clay as to natural sand.

This series of validation experiments reveals that the precision of PIV is a strong function of patch size, L, and is also influenced by image content. The empirically derived curve UB in Fig. 5 is an upper bound on the precision error, ρ_{pixel}, and is given by equation (1). This equation allows a

conservative estimate of the random errors present in subsequent PIV data to be made.

$$\rho_{\text{pixel}} = \frac{0 \cdot 6}{L} + \frac{150\,000}{L^8} \qquad (1)$$

By dividing this error, ρ_{pixel}, by the image width in pixels, the precision can be expressed as a fraction of the FOV.

The selection of an optimum patch size in PIV analysis requires two conflicting interests to be balanced. Larger patches offer improved precision (Fig. 5, equation (1)), whereas smaller patches allow the image to contain a greater number of measurement points, revealing detail in areas of high strain gradient.

CLOSE-RANGE PHOTOGRAMMETRY
Theory

Having obtained image-space deformation data using PIV, these measurements must be converted into object-space coordinates. The coordinate systems for image and object space are defined in Fig. 7. The conversion from pixel coordinates into object-space position is represented by the transformation $U \Rightarrow X$.

Previous image-based deformation systems used in geotechnics, with the notable exceptions of those described by Taylor *et al*. (1998) and Paikowsky & Xi (2000), have used the assumption that a single scale factor can be used to convert between pixel coordinates and object-space position. This assumption is valid only if the camera behaves according to the pinhole model, the object plane is exactly parallel to the CCD plane, and the pixels are square. These assumptions are never all valid in the case of short focal length digital photography. The sources of image distortion, which cause a spatial variation in image scale, are as follows.

Non-coplanarity of the CCD and object planes. If the normals to the CCD and object planes are not parallel, a distorted view of the object plane will be projected onto the CCD. When assembling an experiment, an approximate alignment can be achieved. However, compared with the small errors associated with PIV precision, a slight misalignment of the camera can create a relatively large loss of accuracy. For example, if a camera with a 20° wide FOV is misaligned by 1°, the camera-to-object distance at the edge of the image will be reduced by 0·3%. In other words, a rigid body motion corresponding to 10·00 pixels at the image centre will be seen as 10·03 and 9·97 pixels at the edges of the image.

In the case of centrifuge modelling, even if the camera can be posed correctly prior to the experiment, the increased self-weight of the camera and supporting frame may cause a change in pose. Take (2003) observed a 3° apparent rotation due to distortion of the lens system of a digital still camera when tested at an acceleration of 100 *g*.

Radial and tangential lens distortion. The pinhole camera model, signified in Fig. 7 by a bundle of rays passing straight through a single point to form a perspective projection of the object on the CCD, is an approximation. Radial lens distortion causes light rays to be deflected radially from the normal to the lens (Slama, 1980), and is commonly known as *fisheye*. A second error arises as the centres of curvature of the lens surfaces through which the light is refracted are not always collinear. This is particularly the case for cameras containing multiple lenses, such as compact digital cameras. This second error creates decentring distortion, which has a radial and tangential component. The tangential component is known as *barrelling*.

Refraction through a viewing window. An additional source of image scale variation arises when the object lies behind a viewing window. An apparent variation in object size arises, depending on the thickness and refractive index of the window, and the inclination of the incident rays.

CCD pixel non-squareness. A final source of image scale variation occurs because CCD pixels are not perfectly square. Although this is a small correction, it can be incorporated as a linear scaling factor in the transformation from pixel coordinates to image-space coordinates. The pixel aspect ratio, α, is defined as the height of a pixel divided by the width: it is typically in the range $1 \pm 0 \cdot 004$ (Heikkila & Silven, 1997; Ahmad & Chandler, 1999), and is considered to be constant over the CCD.

$U \Rightarrow X$ transformation

The principles of close-range photogrammetry have been used to develop a more robust transformation $U \Rightarrow X$. Each of the sources of image distortion described above is explicitly modelled, yielding a 14-parameter transformation following Heikkila & Silven (1997), which has been extended to include distortion due to observation through a viewing window. The 14 parameters are as follows:

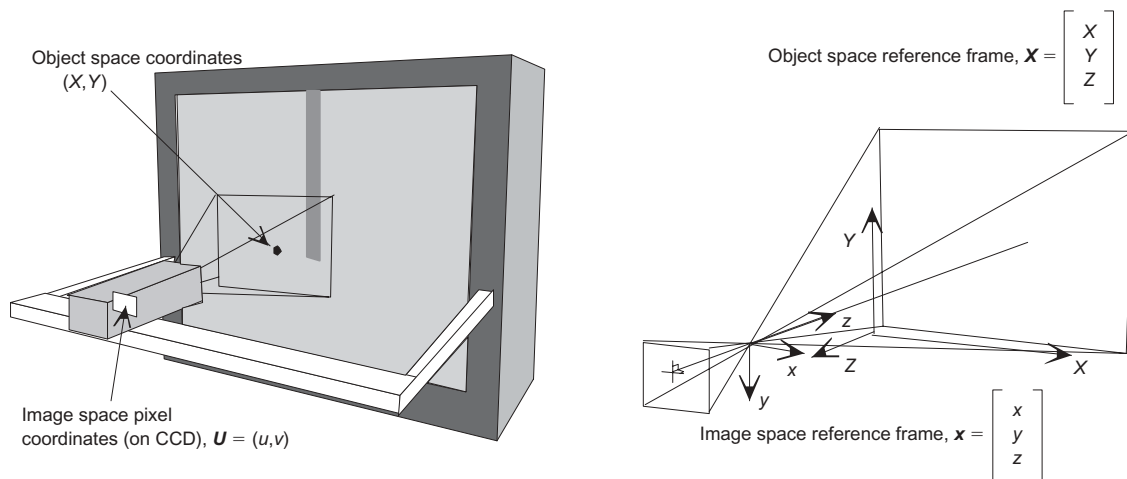(*a*) camera pose: six parameters to describe the translation

Fig. 7. Object-space and image-space coordinate systems

and rotation between the image-space, x, and object-space, X, coordinate systems.
(b) focal length, f
(c) principal point, (u_0, v_0): the pixel coordinates of the intersection of the optical axis and the CCD plane
(d) radial lens distortion (two parameters, k_1, k_2)
(e) tangential lens distortion (two parameters, p_1, p_2)
(f) CCD pixel squareness (α).

In addition to these parameters, the refractive index and thickness of any viewing window(s) are included in the transformation. Snell's law is used to model refraction.

In order to convert a set of image-space coordinates deduced using PIV into object-space coordinates, the 14 transformation parameters are required. These are found by locating the image-space position of a set of reference targets whose object-space coordinates are known. From this set of known U and X coordinates, the transformation parameters can be optimised.

Transformation parameters that do not vary over time, or when the camera is moved between viewing positions, can be found during a single calibration experiment, separate from the experiment in which deformation measurements are to be gathered. Taylor *et al.* (1998) observed that the intrinsic camera parameters (relating to principal point, focal length, and radial and tangential lens distortion) of analogue miniature video cameras do not vary even during centrifuge testing. However, the digital still cameras used in this research suffer significant internal distortion under centrifuge testing. Therefore it proved necessary to deduce all 14 transformation parameters on an image-by-image basis.

The procedure for calibrating a set of image-space coordinates found from PIV is as follows.

Reference target identification. The image-space coordinates of a small number of reference targets, whose object-space coordinates (relative only to each other) have been deduced prior to the experiment, are identified. This identification is carried out by multiple-threshold centroiding (Take, 2003), yielding a precision better than 0·1 pixels for a typical 20×20 pixel reference target. Having identified the location of these targets in the initial image, their subsequent movement is found using PIV.

Transformation optimisation. As the refraction and lens distortion models contain non-linear components, the $U \Rightarrow X$ transformation must be optimised iteratively. A first estimate of the linear parameters is made using a direct linear transformation (Abdel-Aziz & Karara, 1971). These parameters are used as initial values for a Levenberg–Marquardt non-linear optimisation, using the solution method described by Heikkila & Silven (1996). A correction vector masking the influence of refraction is then applied to the first non-linear solution. Improved transformation parameters are found, and the process is repeated until steady values are reached.

Conversion of PIV measurements from image space (U) to object space (X). The deduced transformation parameters are used to convert the image-space coordinates into object-space coordinates. After removing the non-linear lens distortion, a linear camera model is used to establish the object-space measurement coordinates in the absence of refraction. Finally, having established the pose of the camera, a correction vector to account for refraction is applied.

Validation of photogrammetric calibration procedure
The photogrammetric calibration procedure governs the accuracy of this measurement system—that is, the systematic difference between the measured and true coordinates. As image-based measurement systems report an initial position of an object, and its displacement vector between an image pair, two types of accuracy can be defined. *Positional* accuracy is the difference between the reported initial position of an object and its true value. *Movement* accuracy is the difference between the reported displacement vector of an object and its true value.

A series of validation experiments were conducted to assess both the positional accuracy and the movement accuracy of this system. Positional accuracy was assessed by comparing the systematic difference between the true coordinates of a grid of reference targets, and the coordinates calculated from reconstruction of the measured image-space values. A certified photogrammetric reference field consisting of three regular grids of dots provided a reference field of known object-space coordinates (Fig. 8).

The position of each dot within the reference field was located in image space by multiple-threshold centroiding (Take, 2003). Knowing the image- and object-space locations of each dot, the optimal photogrammetric transformation parameters were found. Using these parameters, the object-space coordinates of each dot were estimated from the image-space values, and the discrepancies between these and the true values were found.

Three different images were reconstructed by this method:

Image A: A view of the photogrammetric target with the camera axis nominally normal to the target plane (Fig. 8).
Image B: A view of the photogrammetric target with the camera axis nominally normal to the target plane, seen through a 72 mm layer of Perspex.
Image C: A view of the photogrammetric target with the camera inclined at 20° from normal to the target plane.

In addition, each image was reconstructed using a constant scale factor, as a simple alternative to photogrammetric correction. This is the conventional calibration method that has been used by previous image-based deformation methods, with the exception of Taylor *et al.* (1998) and Paikowsky & Xi (2000). The constant scale factor was chosen such that the mean discrepancy between the measured and actual coordinates was zero, and the standard deviation was minimised.

Table 1 shows the standard deviation of the discrepancy vectors between the measured and actual coordinates. These values demonstrate that the use of photogrammetric calibration improves positional accuracy compared with the use of a constant image scale factor. The transformation $U \Rightarrow X$ for image A is illustrated in Fig. 9 by the spatial variation in image scale in the X and Y directions. This curved surface demonstrates that the apparently regular grid of dots in image A (Fig. 8) contains systematic distortion, which can be captured by the photogrammetric transformation. The bowl-shaped curvature in Fig. 9 arises from radial lens distortion; the asymmetry indicates non-coplanarity of the image and object planes. This non-coplanarity is present despite careful attempts to position the camera axis orthogonal to the target plane.

If the discrepancy vectors for close range photogrammetry summarised in Table 1 are plotted on the original image, their spatial distribution is random, rather than systematic. A systematic distribution of discrepancy vectors would imply that the transformation function $U \Rightarrow X$, which is smooth and continuous and is illustrated by the curved image scale surface in Fig. 9, is unable to shape itself appropriately. This would arise if the optical behaviour of the camera was not captured correctly in the $U \Rightarrow X$ transformation.

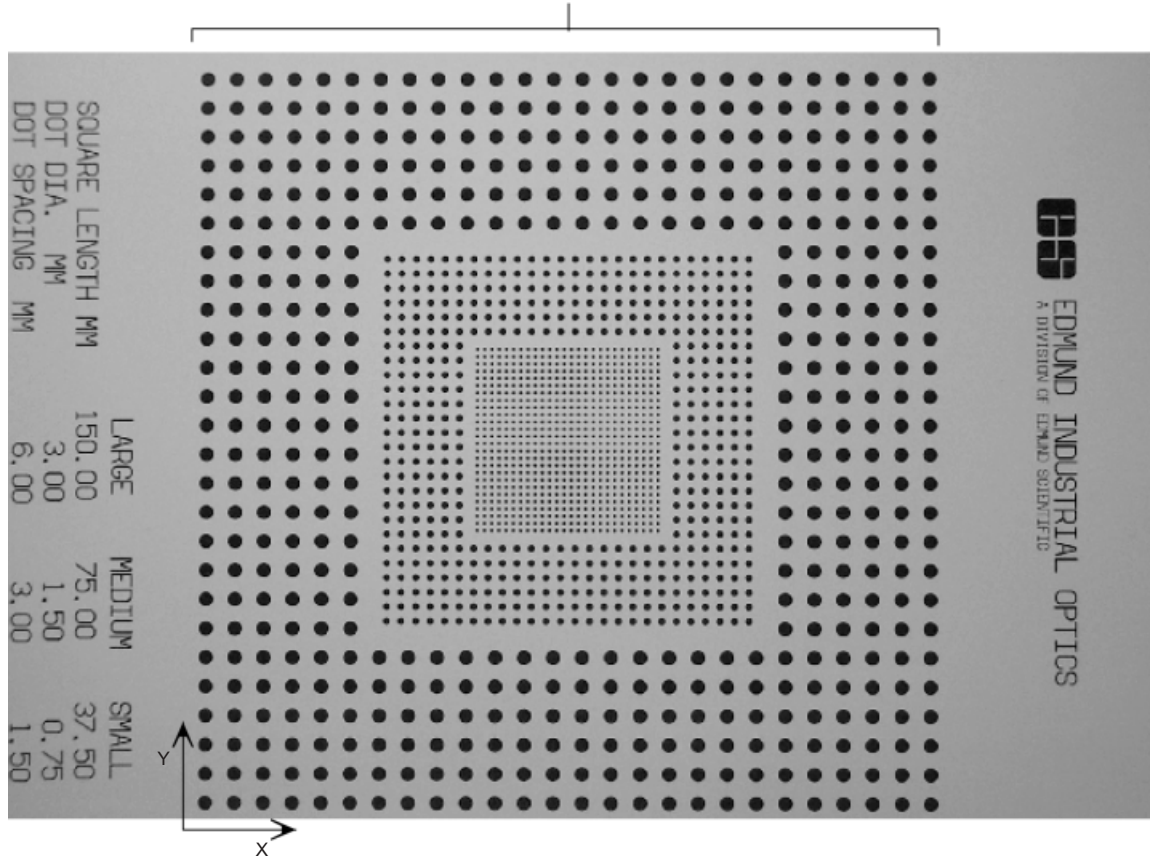Array of 480 3 mm diameter dots, located at 6 mm centres

Fig. 8. Image A: photogrammetric target

Table 1. Standard deviation (μm) between actual and reconstructed location of reference dots

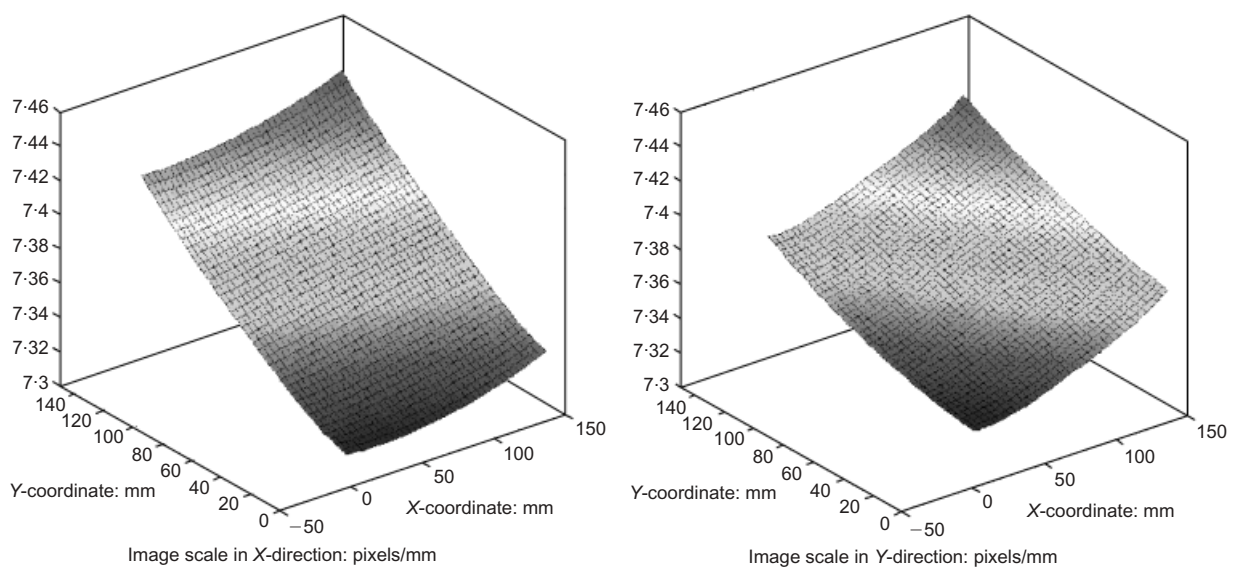| Reconstruction method	Image A		Image B		Image C	
Direction	X	Y	X	Y	X	Y
Close-range photogrammetry	7·4	8·6	8·8	9·0	9·4	7·3
Linear scaling	25·1	33·2	19·4	24·9	246·4	128·8

Fig. 9. Image A: spatial variation in image scale

Linear scaling, for example, could be depicted by a horizontal surface in Fig. 9, leading to a systematic spatial distribution in discrepancy between the assumed image scale and the actual image scale, and hence a systematic spatial distribution in positional error.

The random spatial distribution of the discrepancy vectors indicates that the discrepancy errors do not arise from the photogrammetric calibration routine. Instead, the errors lie in the underlying data of the image- and object-space locations of the reference dots. Therefore the positional accuracy of this system is not limited by the calibration routine, but by either the multiple-threshold centroiding method used to locate the reference targets or the accuracy of the photogrammetric reference field itself.

The *movement* accuracy of the system is defined as the difference between the true and measured values of an object-space displacement vector of a single patch found from comparison of two images. This discrepancy arises from the error in the PIV image-space displacement measurement (estimated from equation (1)) and the change in the $U \Rightarrow X$ transformation created by the error in the measured movement of the reference markers (which are also found using PIV, and can be estimated from equation (1)). These two additive errors can be summed geometrically. In the case of $L = 32$, which corresponds to the patch size used to track the 3 mm dots in Fig. 8, these errors sum to 0·0265 pixels, or 1/66374th of the FOV.

This definition of movement accuracy is supported by a further validation exercise. The photogrammetric reference field shown in Fig. 8 was translated over a distance of 6 pixels below a stationary camera. A subset of 20 dots from the array of 480 3 mm diameter dots was selected to represent reference markers in a typical experiment. These reference markers are used to define the object-space reference frame. As the photogrammetric target was translated, not distorted, the movement of the 460 remaining dots relative to the 20 reference dots should be equal to zero.

The movement of each of the 480 dots was tracked using PIV patches of size 32×32 pixels, yielding initial and displaced image-space coordinates for each dot. The subset of 20 dots was used to evaluate the photogrammetric transformation for the initial and displaced images, and these transformation parameters were used to evaluate the object-space displacement vectors of the remaining dots. The mean discrepancy between the true displacement of zero and the measured values was found to be 2 μm. Noting that the field of view was 240 mm, this error corresponds to a normalised

movement accuracy better than 1/100 000th. This accuracy exceeds the value predicted by equation (1), confirming that this offers a conservative estimate of measurement error.

The observation that movement accuracy (that is, the accuracy by which displacement vectors are evaluated) can exceed positional accuracy can be illustrated as follows. The actual and measured locations of a single stationary reference target and a nearby soil element in two images are shown schematically in Fig. 10. As discussed earlier, the errors associated with reference target location using multiple threshold centroiding are larger than the random errors in displacement measurements made using PIV. Fig. 10 shows a discrepancy between the actual and measured initial coordinates of the reference marker, introduced by the centroiding procedure. This discrepancy vector is carried through to the transformation $U \Rightarrow X$, leading to a similar *positional* error in locating the nearby soil element.

However, the error in the measured *movement* of the soil element is smaller. The movements of the reference marker and the soil element between the initial and displaced images are measured using PIV. The discrepancy vector introduced when locating the reference marker is carried through unchanged, contributing zero error over the movement step. Therefore the error in the movement vector arises only from PIV measurements of the soil and reference marker, which can be summed geometrically. The initial error introduced while locating the reference target does not influence the measured displacement vector.

System performance

The overall performance of this measurement system can be quantified by

(*a*) precision
(*b*) accuracy (positional and movement)
(*c*) the size of the array of measurement points that can be contained within a single view.

The precision of this system derives from the PIV technique, is a strong function of PIV patch size, L, and can be conservatively estimated from equation (1).

The positional accuracy of the system depends on the method used to establish the image-space location of the reference targets. Multiple-threshold centroiding allows the image-space location of a typical reference target (30×30 pixels) to be established to an accuracy better than 0·1 pixels. For the 2-megapixel digital still camera used in this
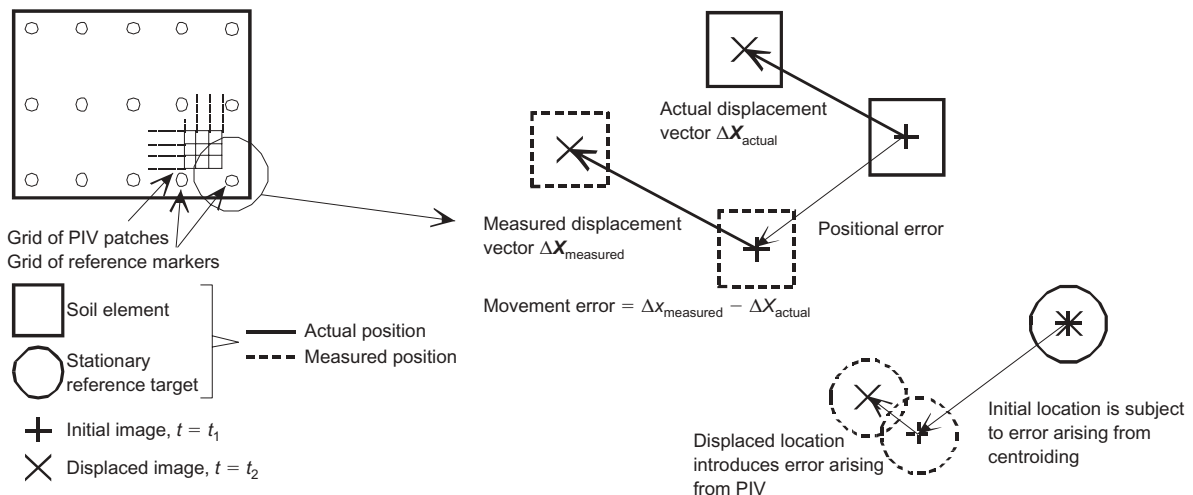

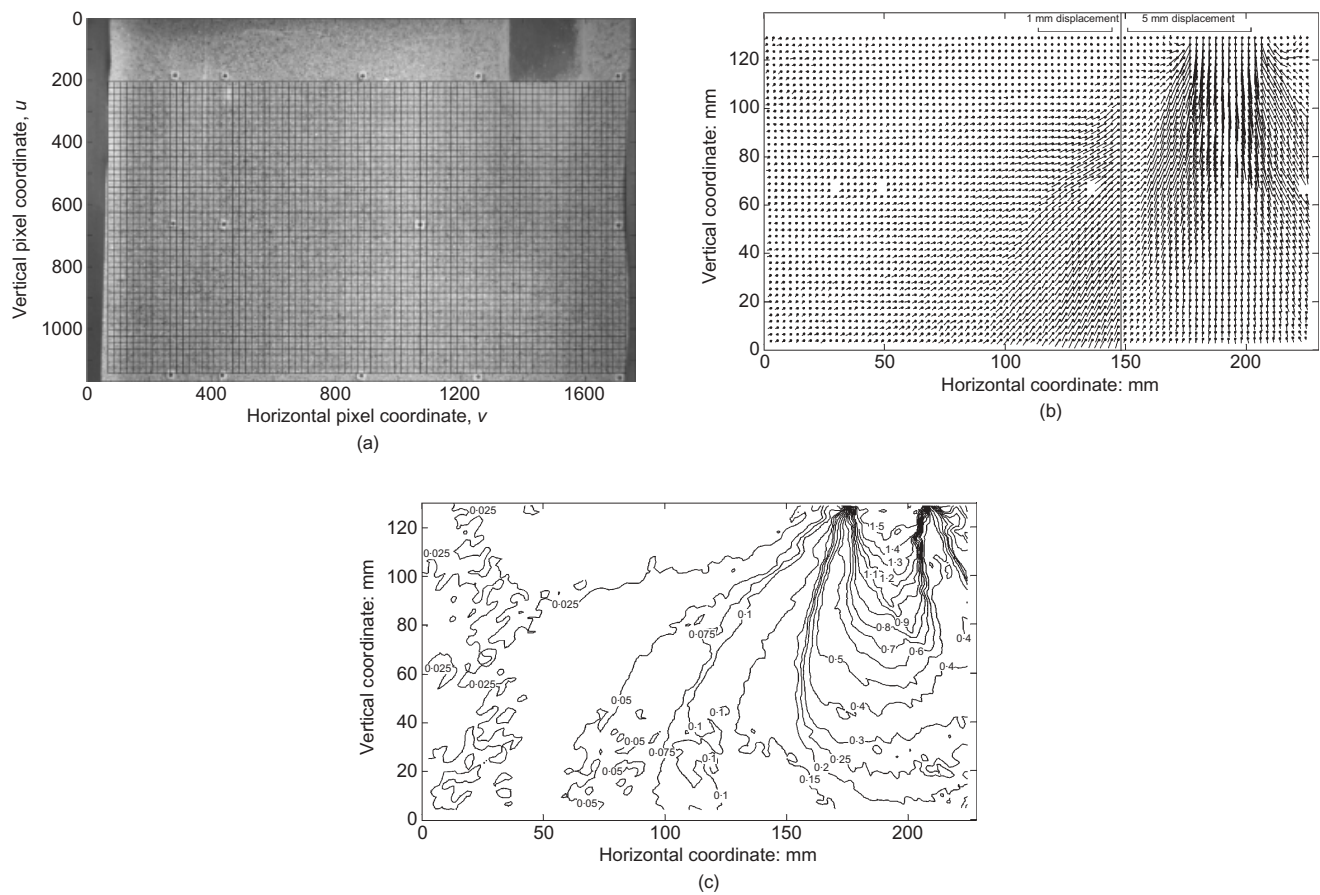Fig. 10. Positional and movement accuracy

Fig. 12. Displacement field around plane strain displacement pile in sand: (a) mesh of PIV patches; (b) displacement vector field; (c) magnitude of displacement vectors
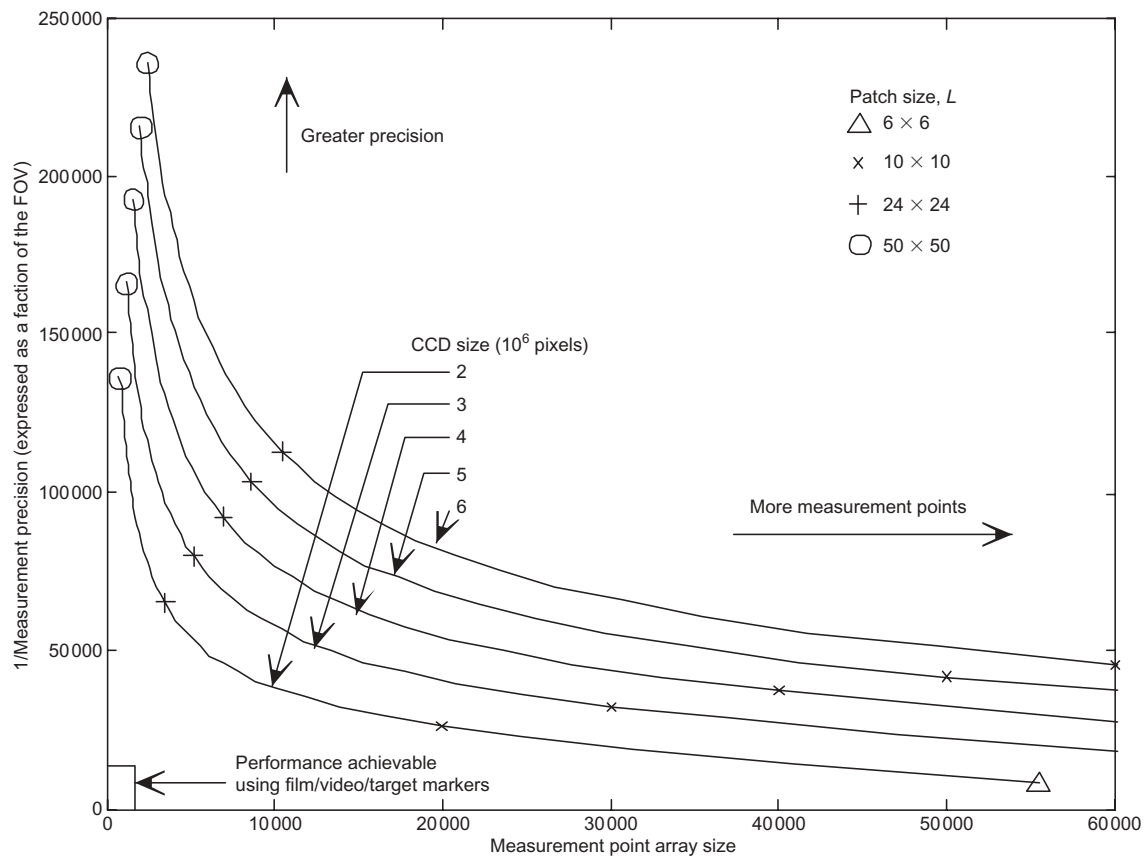

Fig. 11. Precision against measurement array size

research (1760 × 1168 pixel resolution), this accuracy corresponds to 1/17 600th of the FOV.

The movement accuracy of the system derives from the errors of the PIV operations used to (a) track the soil in image space, and (b) track the reference targets from which the image-space to object-space transformation parameters are derived. In both cases the errors are a strong function of the PIV patch size (equation (1)). Geometric summation of the errors yields an estimate of the movement accuracy. This estimate agrees closely with the results of a validation exercise.

The number of measurement points that can be established in an image is a function of the PIV patch size. By using smaller PIV patches, the measurement array size can be increased, at a cost of reduced precision. Fig. 11 shows the relationship between precision and measurement array size for different resolutions of camera CCD, based on the empirical estimate of precision provided by equation (1).

EXAMPLE APPLICATIONS

The performance of this system is illustrated with two example applications. Fig. 12(a) shows a view through the window of a plane-strain calibration chamber used to simulate the installation of a displacement pile (White, 2002). A mesh of 3201 PIV patches overlies the soil below the tip of the 32·2 mm wide model pile. Visible in the image are the 14 reference targets used to optimise the photogrammetric transformation parameters. This image is compared with a subsequent image captured after 1·5 mm of pile movement. PIV analysis of the two images followed by photogrammetric calibration reveals the displacement field shown in Fig. 12(b).

To reveal the zone of deformation, contours of displacement vector magnitude are shown in Fig. 12(c). The fine mesh of PIV patches is able to capture the high velocity gradient close to the pile tip, while also revealing the very small movements in the far field.

In the second example application, the imaging system is used to observe the onset of progressive failure in a model clay embankment (Take, 2003). Of the three cameras used to record the displacement fields, only the camera focused on the crest of the embankment is presented in Fig. 13(a). This image, taken moments before gravity turn-on, is different from those captured at elevated acceleration levels. In the centrifuge environment, the camera lens acts as a cantilever, which deflects according to its increased self-weight. Thus the downwards rotation of the camera lens with respect to the object plane results in an apparent largely upwards displacement of the PIV patches, in this case approaching 100 pixels for the gravity turn-on to 60g (Fig. 13(b)). PIV analysis of the 20 reference targets provides the basis to extract the soil movement from the camera movement and distortion by tracking the displacement vectors of the stationary targets (Fig. 13(c)). Finally, photogrammetric calibration reveals the hidden soil movement during consolidation (Fig. 13(d)) necessary to describe the initial state of the model, which had been dwarfed by the gravity-induced changes in the calibration parameters.
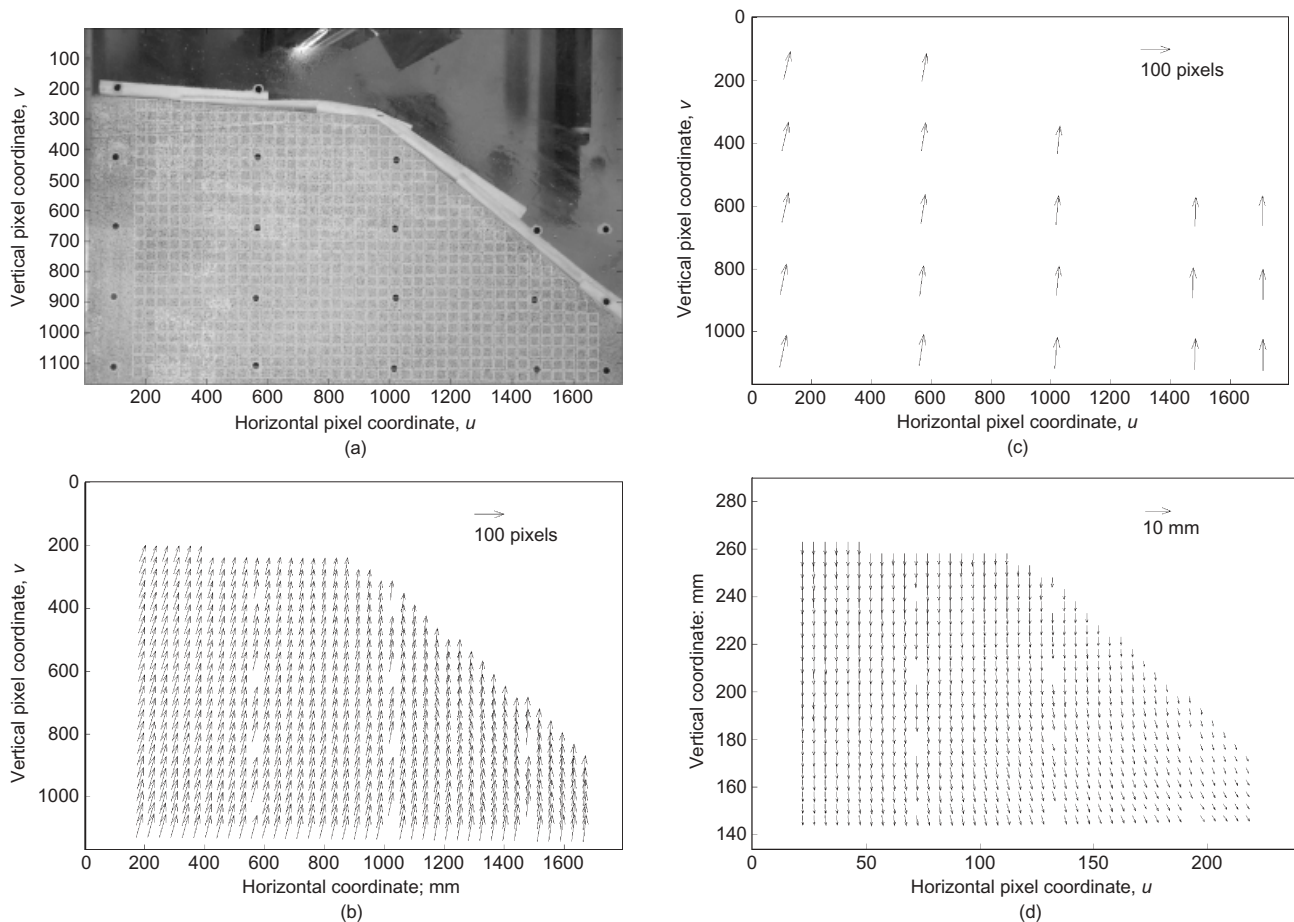

Fig. 13. Determination of displacement vectors during gravity turn-on to 60g using close-range photogrammetry: (a) mesh of PIV patches at crest of model embankment; (b) observed image-space vector field during gravity turn-on to 60g; (c) observed image-space displacements of stationary reference markers; (d) actual object-space consolidation settlement

CONCLUSIONS

A new system for measuring deformation in geotechnical tests based on digital photography, particle image velocimetry (PIV) and close-range photogrammetry is presented. Compared with previous image-based methods of displacement measurement, this system offers an order-of-magnitude increase in accuracy, precision, and measurement array size. This performance is achieved using a relatively inexpensive (< £300) 2-megapixel digital still camera. In the future, the availability of higher-resolution CCDs at lower cost will lead to corresponding increases in performance (Fig. 11).

REFERENCES

Abdel-Aziz, Y. I. & Karara, H. M. (1971). Direct linear transformation into object-space coordinates in close-range photogrammetry. *Proceedings of the symposium on close-range photogrammetry, Urbana*, Vol. 1, p. 1–18.

Adrian, R. J. (1991). Particle imaging techniques for experimental fluid mechanics. *Ann. Rev. Fluid Mech.* **23**, 261–304.

Ahmad, A. & Chandler, J. H. (1999). Photogrammetric capabilities of the Kodak DC40, DCS420 and DCS460 digital cameras. *Photogramm. Rec.* **16**, No. 94, 601–615.

Andrawes, K. Z. & Butterfield, R. (1973). The measurement of planar displacements of sand grains. *Géotechnique* **23**, No. 5, 571–576.

Butterfield, R., Harkness, R. M. & Andrawes, K. Z. (1970). A stereo-photogrammetric technique for measuring displacement fields. *Géotechnique* **20**, No. 3, 308–314.

Heikkila, J. & Silven, O. (1996). Calibration procedure for short focal length off-the-shelf CCD cameras. *Proc. 13th Int. Conf. Pattern Recognition, Vienna*, 166–170.

Heikkila, J. & Silven, O. (1997). A four-step camera calibration procedure with implicit image correction. *Proc. IEEE Computer Soc. Conf. Computer Vision and Pattern Recognition (CVPR'97), San Juan*, 1106–1112.

Paikowsky, S. G. & Xi, F. (2000). Particle motion tracking utilizing a high-resolution digital CCD camera. *ASTM Geotech. Test. J.* **23**, No. 1, 123–134.

Phillips, R. (1991). *Film measurement machine user manual*. Cambridge University Technical Report, CUED/D-Soils/TR 246.

Roscoe, K. H., Arthur, J. R. F & James, R. G. (1963). The determination of strains in soils by an X-ray method. *Civ. Engng Public Works Rev.* **58**, 873–876, 1009–1012.

Scholey, G. K., Frost, J. D., Lo Presti, D. C. F. & Jamiolkowski, M. (1995). Review of instrumentation for measuring small strains during triaxial testing of soil specimens. *ASTM Geotech. Test. J.* **18**, No. 2, 137–156.

Slama, C. C. (ed.) (1980). *Manual of photogrammetry*, 4th edn. American Society of Photogrammetry, VA, USA.

Take, W. A. (2003). *The influence of seasonal moisture cycles on clay slopes*. PhD dissertation, University of Cambridge.

Taylor, R. N., Grant, R. J., Robson, S. & Kuwano, J. (1998). An image analysis system for determining plane and 3-D displacements in soil models. *Proc. Centrifuge '98*, 73–78. Tokyo.

White, D. J. (2002). *An investigation into the behaviour of pressed-in piles*. PhD dissertation, University of Cambridge.